Structure and dynamics of condensed multivalent ions within polyelectrolyte bundles: a combined x-ray diffraction and solid-state NMR study

Thomas E Angelini[1]**, Lori K Sanders**[2]**, Hongjun Liang**[2]**, Willy Wriggers**[3]**, Jay X Tang**[4] **and Gerard C L Wong**[1,2]

[1] Department of Physics, University of Illinois at Urbana-Champaign, IL 61801, USA
[2] Department of Materials Science and Engineering, University of Illinois at Urbana-Champaign, IL 61801, USA
[3] School of Health Information Sciences, University of Texas Health Science Center at Houston, 7000 Fannin Street Suite 600, Houston, TX 77030, USA
[4] Department of Physics, Brown University, Providence, RI 02912, USA

E-mail: gclwong@uiuc.edu

Abstract
Like-charged polyelectrolytes can attract and condense into compact ordered states via counterion-mediated interactions (Gelbart *et al* 2000 *Phys. Today* **53** 38–44). Recent examples include DNA toroids and F-actin bundles. We have investigated the structure and dynamics of condensed divalent ions within F-actin polyelectrolyte bundles. Using synchrotron x-ray diffraction, the structural organization of Ba^{2+} ions on F-actin has been directly observed. The Ba^{2+} ions organize into counterion charge density waves (CDWs) parallel to the actin filaments. Moreover, these 1D counterion charge density waves couple to twist deformations of the oppositely charged actin filaments, and mediate attractions by effecting a 'zipper-like' charge alignment between the counterions and the polyelectrolyte charge distribution. We have also examined condensed divalent ^{25}Mg ions within F-actin bundles using solid-state NMR. Preliminary measurements indicate that the longitudinal relaxation time T_1 of Mg^{2+} ions decreases by approximately an order of magnitude as they organize into the CDW state within condensed F-actin bundles. The measured value of T_1 for Mg^{2+} ions in the CDW is intermediate between typical liquid-like and solid-like values.

(Some figures in this article are in colour only in the electronic version)

1. Introduction

Electrostatics in aqueous media is often understood in terms of mean field theories such as the Poisson–Boltzmann formalism [2–4], in which like-charged objects such as polyelectrolytes

always repel. Indeed, DNA chains in water containing monovalent ions always repel one another. Linearized versions of mean field theory provide the theoretical underpinning for widely employed tools such as Debye–Hückel theory and DLVO (Derjaguin–Landau–Verwey–Overbeek) theory [5, 6], which constitute the usual starting point for understanding charged polyelectrolyte or colloidal systems.

In systems with strong electrostatic interactions (containing, for example, high surface charge densities, multivalent ions, etc), however, the physics is qualitatively different. Interactions between polyelectrolytes can be controlled by the structure and dynamics of the condensed ions surrounding the polyelectrolyte. It has been recognized for some time that the mean field Poisson–Boltzmann approach cannot produce attractions unless some form of correlation between counterions is introduced [7–9]. As Kirkwood [8] suggested and Oosawa [9] showed using an approximate analytical model, like-charged attractions between polyelectrolytes may be possible due to the correlated fluctuations of the condensed ion layers around strongly charged polyelectrolytes. A large number of theoretical investigations have focused on the existence and form of multivalent ion induced like-charge attraction between cylindrical polyelectrolytes [10, 11].

Recently, a number of anionic biopolymers (with persistence lengths of 1 μm or more) have been used as experimental systems for the study of like-charge polyelectrolyte attraction, such as the filamentous bacteriophages, microtubules, and F-actin [12, 13]. Due to their large persistence lengths, they can be thought of as idealized rod-like polyelectrolytes, and a number of interesting new effects have been found. For example, in the presence of divalent ions, F-actin progressively condenses into close-packed bundles via an intermediate state comprised of 1D lamellar stacks of liquid crystalline actin networks [14–16]. The dependence of DNA and actin condensation on ion valence, size, and structure has been systematically studied experimentally [12, 17] and an empirically motivated criterion for the valence dependence has been proposed based on experimental results for 'dumbbell' divalent ions [18].

Polyelectrolytes in aqueous solution are coated by a condensed 'Manning' layer of mobile oppositely charged counterions [19]. All proposed theoretical explanations for like-charge attraction introduce some form of positional counterion correlations within this layer. For example, dynamic 'van der Waals'-like correlations of long-wavelength ion fluctuations have been suggested [8, 9, 20–23]. Static mechanisms consisting of ion correlations along the axis of the polyelectrolyte rods in the form of a Wigner lattice have also been considered [24–27]. Recently, theoretical models based on discretized distributions of condensed ions on polyelectrolytes have been solved analytically and numerically [28–30].

We have investigated the structure and dynamics of condensed divalent ions within F-actin polyelectrolyte bundles. The organization of multivalent ions on actin filaments has been directly measured using synchrotron x-ray diffraction [31]. The counterions do not form a lattice that simply follows actin's helical symmetry; rather, they organize into one-dimensional (1D) charge density waves parallel to the actin filaments (figure 1). Moreover, this 1D counterion charge density wave forms a coupled mode with torsional distortions of the oppositely charged polyelectrolyte. We have also performed solid-state NMR experiments on condensed divalent ions within F-actin bundles. Preliminary measurements of the longitudinal relaxation time T_1 show that Mg^{2+} ions condensed in F-actin bundles are much less mobile that those in solution.

2. Experimental details

Small angle x-ray scattering (SAXS) measurements were performed using both an in-house x-ray source as well as beam line 4-2 at the Stanford Synchrotron Radiation Laboratory
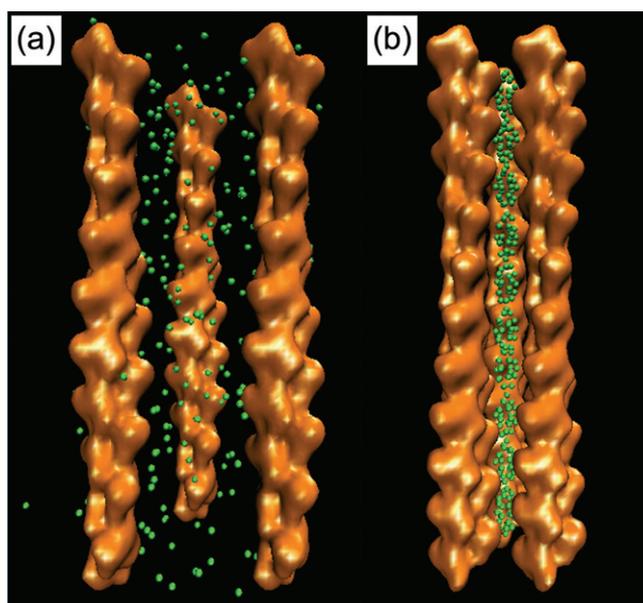
Figure 1. Schematic representations of uncondensed and condensed F-actin. (a) At low multivalent ion concentrations, three F-actin filaments maintain their native $-13/6$ symmetry, and are unbound. (b) At high multivalent ion concentrations, the ions collectively form a charge density wave (CDW) and 'bundle' F-actin filaments. Moreover, the CDW forms a coupled mode with torsional distortions of the F-actin, and has overtwisted it by $-3.8°$ per monomer to a new $-36/17$ symmetry. The representations of F-actin are low-resolution density maps generated using Situs software (http://situs.biomachina.org/).

(SSRL, Palo Alto, CA). For the in-house experiments, incident Cu Kα radiation ($\lambda = 1.54$ Å) from a Rigaku (The Woodlands, TX) rotating-anode generator was monochromatized and focused using Osmic (Auborn Hills, MI) confocal multilayer optics, and scattered radiation was collected on a Bruker AXS (Madison, WI) 2D wire detector (pixel size $= 105~\mu$m). For the SSRL experiments, incident synchrotron x-rays from the BL-4-2 eight-pole wiggler were monochromatized to 8.98 keV using a double-bounce Si(111) crystal ($\lambda = 1.3806$ Å), and focused using a cylindrical mirror. The scattered radiation was collected using a MAR Research (Evanston, IL) charge-coupled device camera (pixel size $= 79~\mu$m). The 2D SAXS data from both set-ups have been checked for mutual consistency.

In general, diffraction features generated by counterion correlations are expected to be weak compared with those generated by biopolymer organization. To detect positional correlations in counterion distributions on the surface of a charged polymer using SAXS, a number of experimental strategies have been employed. For polyelectrolytes with small diameters and thereby high surface curvatures, or for polyelectrolytes that are very flexible, we hypothesized that counterion correlations will be broken up into small domains, and the resultant diffraction peaks will correspondingly broaden and become difficult to distinguish from the background of scattering, which have a number of contributions, including polyelectrolyte organization and form factor effects. Filamentous actin (F-actin) was chosen as a model system because it is a rigid polyelectrolyte (persistence length $\xi_A = 10~\mu$m) with a large diameter ($D_A = 75$ Å) [32, 33], so that counterion correlations can have the potential to form large domains, and thereby generate sharp, detectable peaks. Because the number of atoms that comprise the charged biopolymer is large compared with the number of

counterions, high molecular weight counterions (Ba^{2+}) were used to improve the Z-contrast between counterion scattering and biopolymer scattering. Finally, to further highlight the diffraction features that are generated by the counterions, we compared the SAXS patterns from F-actin that has been concentrated non-electrostatically (with no added multivalent ions) with F-actin that has been condensed electrostatically by using multivalent ions.

In order to do this experiment, it was necessary to obtain at least partially aligned samples, so that correlations along different directions can be discerned. The best alignment of the F-actin biopolymer is usually achieved in samples with monovalent ion based buffers such as those typically employed in typical structural biology experiments, and in non-electrostatically concentrated samples, such as those used in our control experiments. Unlike those samples, however, multivalent ion condensed biopolymer samples typically exhibit poor alignment because of the existence of ion mediated strong attractions that cause the precipitation of the F-actin. Typically, the precipitated F-actin is compacted into a dense pellet during mixing. These pellets consist of many coexisting domains of actin bundles locally oriented along different random directions, which leads to 'powder averaging' of the diffraction pattern and the associated loss of orientational information. In order to minimize these effects, we use a small ($300 \times 300 \ \mu m^2$) x-ray beam to get diffraction information on locally aligned domains within a pellet.

The most abundant intracellular protein in eukaryotic cells is actin, one of the principal components of the cytoskeleton. Actin associates to form polymeric actin filaments, which can in turn form bundles and networks in a highly coordinated way by interacting with actin binding proteins and salts. The actin cytoskeleton determines cell shape, and plays a central role in cellular locomotion [32]. Monomeric actin (G-actin) (MW 43 000) was prepared from a lyophilized powder of rabbit skeletal muscle purchased from Cytoskeleton, Inc. (Denver, CO). The non-polymerizing G-actin solution contained a 5 mM Tris buffer at pH 8.0, with 0.2 mM $CaCl_2$, 0.5 mM ATP, 0.2 mM DTT, and 0.01% NaN_3. G-actin (2 mg ml^{-1}) was polymerized into F-actin (linear charge density $\lambda_A \approx -1e/2.5$ Å at pH 7) with the addition of salt (100 mM KCl final concentration). F-actin rods are comprised of G-actin monomers packed into a helix with a $-13/6$ symmetry, or 13 monomers in six left handed helical turns. Each G-actin monomer has dimensions of approximately 55 Å $\times$ 55 Å $\times$ 35 Å, and is comprised of four subdomains. For the purpose of modelling x-ray diffraction from actin filaments, these four subdomains can be approximated as four spheres with appropriate radii and molecular weights [34]. Human plasma gelsolin, an actin severing and capping protein (Cytoskeleton, Inc.), was used to regulate the F-actin length. The average length of F-actin is controlled by the gelsolin concentration, which has been independently calibrated [35]. The filaments were treated with phalloidin (MW 789.2; Sigma Aldrich, St. Louis, MO) to prevent F-actin depolymerization. F-actin gels were ultracentrifuged at 100 000 g for 1 h to pellet the filaments. After the removal of the supernatant buffer solution, the F-actin was resuspended to a final concentration of 10 mg ml^{-1} by using Millipore H_2O (18.2 MΩ). Electrostatically condensed samples were prepared by mixing with $MgCl_2$ or $BaCl_2$ salt solutions. Non-electrostatically concentrated samples were prepared by ultracentrifugation ($100\,000 \times g$) of F-actin solutions. The supernatant buffer was subsequently removed, and the actin concentration set by the addition of 5 mM pH 7.0 PIPES buffer. All samples were sealed in 1.5 mm diameter quartz capillaries.

The progressive condensation of F-actin bundles with increasing multivalent ion concentrations can be observed in figure 2. F-actin condenses into intermediate state comprised of 1D lamellar stacks of liquid crystalline actin networks before condensing into close-packed bundles [14–16]. SAXS measurements of F-actin bundles condensed with Ba^{2+} exhibit an actin–actin close-packing peak characteristic of the bundled phase at $q = 0.089$ Å^{-1}, which
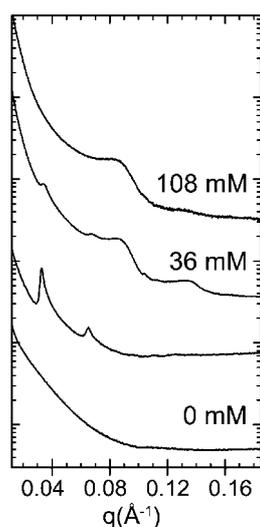
Figure 2. SAXS profiles of F-actin ($\sim$0.2 μm long) condensed by Ba^{2+} ions. At 0 mM Ba^{2+} concentration, F-actin is in an uncondensed isotropic phase. At low Ba^{2+} concentrations (6 mM), F-actin condenses into a network phase, consisting of lamellar stacks of 2D nematic layers. At high Ba^{2+} concentrations (108 mM), an attractive force condenses F-actin into close packed bundles with a correlation peak at $q = 0.089$ Å^{-1}. A weak higher order reflection can also be observed at $q = 0.136$ Å^{-1}, which deviates slightly from the position expected from an exact hexagonal lattice.
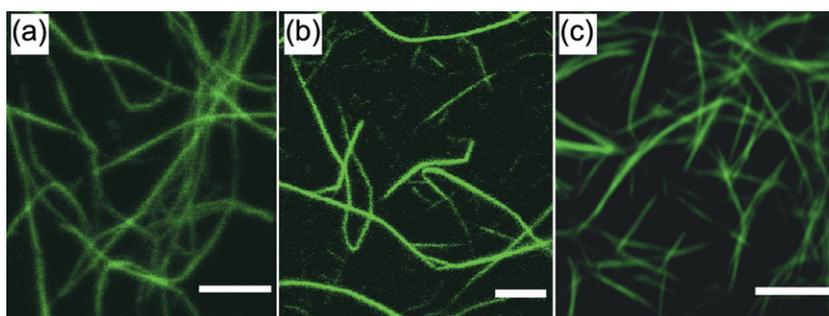
Figure 3. Confocal images of dilute (0.03 mg ml^{-1}) solutions of bundles of F-actin. (a) Mean filament length of $\sim$10 μm at 72 mM global Ba^{2+} concentration. (b) Mean filament length of $\sim$3 μm at 18 mM global Ba^{2+} concentration. (c) Mean filament length of $\sim$0.1 μm at 72 mM global Ba^{2+} concentration. Scale bars are 8 μm.

corresponds approximately to the hard-core diameter of F-actin. These F-actin bundles can also be imaged in real space by using laser-scanning confocal fluorescence microscopy (figure 3). The F-actin filaments were labelled with phalloidinated Alexa Fluor 488 (Molecular Probes, Eugene, OR). A Leica SP-2 confocal microscopy system (Beckman Institute, Urbana, IL) was used to image the dilute F-actin solutions in sealed sample cells at different ionic strengths. The observed thickness of bundles in the image, accounting for the $\sim$0.25 μm point spread function of the microscope, indicates that each bundle is comprised of thousands of filaments.

A direct comparison between the 2D SAXS patterns of F-actin concentrated osmotically without using divalent ions and of F-actin condensed electrostatically with divalent ions is
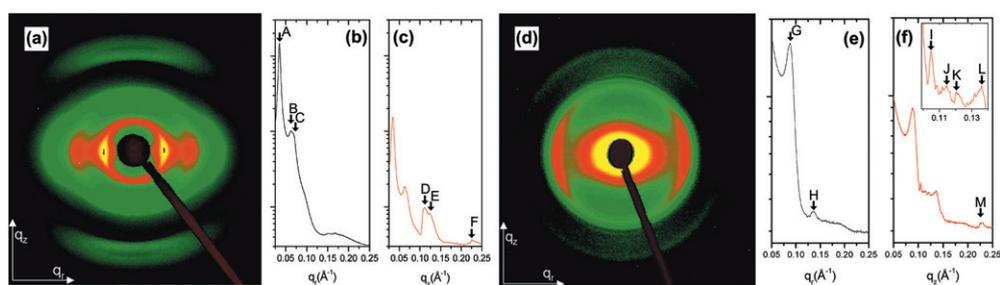
Figure 4. (a) A 2D SAXS pattern of non-electrostatically condensed F-actin. The procedure for generating integrated cuts along q_r (b) and along q_z (c) is described in the text. Peak positions for all observed layer lines (sixth, seventh, and 13th) agree with the native $-13/6$ actin model to within less than 1%. (d) 2D SAXS pattern of Ba^{2+} condensed F-actin. Cuts along q_r (e) and along q_z (f) are performed in the same way. The data indicate the formation of a counterion 1D CDW, and an induced $-3.8°$ overtwist of F-actin (see text). The peak positions are (A) 0.035 Å^{-1}, (B) 0.062 Å^{-1}, (C) 0.07 Å^{-1}, (D) 0.111 Å^{-1}, (E) 0.123 Å^{-1}, (F) 0.225 Å^{-1}, (G) 0.089 Å^{-1}, (H) 0.136 Å^{-1}, (I) 0.105 Å^{-1}, (J) 0.115 Å^{-1}, (K) 0.120 Å^{-1}, (L) 0.136 Å^{-1}, and (M) 0.227 Å^{-1}. The inset is a magnification of the CDW peak (I) and neighbouring layer-line scattering (J, K).

made in figure 4. A large number of different osmotically concentrated F-actin samples were analysed. Figure 4(a) is a representative 2D SAXS pattern of partially aligned F-actin at 90 mg ml^{-1} in the absence of divalent ions. The F-actin rods are partially aligned along the q_z axis and are powder averaged in the plane perpendicular to the q_z axis. In the region of interest in reciprocal space the small angle approximation is valid, so the relationship between detector positions and q positions is greatly simplified. For the analysis of the 2D SAXS patterns (figures 4(a) and (d)), cuts along q_r and q_z are produced by integrating the 2D SAXS image over 40° wedges in χ (χ is the angle between q and q_r), centred about the q_r and q_z axes, where $q_r \equiv q \cos \chi$, $q_z \equiv q \sin \chi$, $q = (4\pi/\lambda) \sin \theta$, and 2θ is the Bragg angle. The three equatorial peaks (A–C) in figure 4(b) correspond to the first-order, $\sqrt{3}$-order, and second-order peaks expected from local hexagonal coordination. The two strong, partially orientationally averaged peaks (D and E) along the meridional direction (figure 4(c)) are the well known sixth- and seventh-layer lines characteristic of $-13/6$ symmetry [36], in agreement with the known structure of F-actin. To account for the sample mosaic and the effects of integration on layer lines, we partially powder averaged ($\pi/2 \geqslant \chi \geqslant \pi/4$) theoretical 2D diffraction patterns. The resulting modelled peak positions have been optimized by varying the monomer spacing in 0.1 Å increments. These peak positions and combined full width at half-maximum are well described (to within 1%) by a Fourier transform of the standard four-sphere model [34] for the actin filament, using the Holmes coordinates [36], combined with Gaussian layer line profiles [37].

The diffraction pattern for multivalent ion condensed F-actin bundles differs dramatically from that of the non-electrostatically concentrated F-actin. Figure 4(d) is a 2D SAXS pattern of a partially aligned sample of F-actin at 7.5 mg ml^{-1} condensed with 60 mM Ba^{2+}. The filaments are oriented parallel to q_z on average as in the non-electrostatically concentrated sample above. The most salient difference between the two diffraction patterns (between figures 4(a) and (d) and between figures 4(c) and (f)) is the appearance of a sharp diffraction feature at $q_z = 0.105$ Å^{-1} in the electrostatically condensed case (figure 4(f), peak I). This finding is surprising because the sample alignment is weaker for the electrostatically condensed actin compared with the non-electrostatically condensed actin, and weaker alignment can only broaden and weaken existing peaks, never produce new ones.

   This peak is centred on the q_z axis and, given the symmetry of the system, is dominated by a zeroth order Bessel function contribution, and is partially smeared in χ. However, no plausible changes in filament symmetry can produce new layer lines with zeroth order Bessel function contributions. (In principle, it may be possible to generate a diffraction peak at this position if one is to *double* the monomer spacing along a filament, but this will no longer be an F-actin helix.) It is therefore not possible to generate this new peak by using the F-actin helix. This new diffraction peak, which only occurs for multivalent ion condensed samples and is aligned along the q_z-axis, corresponds to 'ripples' of multivalent ion density along the filament axis, analogous to a classical 1D charge density wave (CDW). Compared to any of the F-actin layer-line peaks in this region of reciprocal space, this peak is symmetrical, significantly sharper, and more intense. This peak is consistent with the diffraction from a new 1D periodic charge distribution with a finite in-plane width and azimuthal symmetry. The Fourier transform of this charge distribution is a periodic arrangement of Bragg sheets multiplied by zeroth order Bessel functions centred on the q_z axis, which suppress the off-axis Bragg sheet intensity. Unlike the higher order Bessel function peaks from the F-actin helix, which are shifted and broadened along q_z by the large mosaic distribution of bundle orientations within the sample volume, this peak remains sharp along q_z even after such orientational averaging. Because we observe a single peak, the counterion CDW is dominated by one Fourier component and is approximately described by a simple sinusoidal density variation with a spatial period of 59.8 Å, which is comparable to the spacing between monomer ridges on the surface of one side of an F-actin filament. Because of the weak diffraction signal of the CDW, we cannot rule out the possibility of higher harmonics. Our results, however, suggest that the dominant Fourier component of the CDW is the one at $q_z = 0.105\,\text{Å}^{-1}$, which implies that the counterion distribution can be approximated by a 'frozen' 1D sinusoidal ripple along the F-actin helix axis. In samples where divalent ions are progressively removed from the F-actin bundles, the CDW diffraction feature disappears. We recently performed experiments in which the condensed divalent ions are displaced by titrating in low molecular weight multivalent globular proteins such as lysozyme (+9 charge). As the divalent ions in the CDW are displaced by the higher valence lysozyme, the CDW scattering signal is suppressed as expected [38].

   This simple picture, however, is incomplete. For example, why do the counterions follow a new 1D symmetry rather than the full helical symmetry of the charge distribution on F-actin? In principle, if the positively charged divalent ions were to simply follow the negative charge on F-actin, the ion distribution should precess helically with the same symmetry as the F-actin helix, modify the existing Bessel function scattering and generate no new peaks. This is not the case, since we clearly observe the CDW diffraction peak centred on the q_z axis. The question can be resolved if we examine the diffraction pattern from the multivalent ion condensed F-actin, which reveals that the 1D CDW has enforced a change in the native F-actin symmetry and overtwisted the F-actin helix by $-3.8°$ per monomer. This can be seen by the direct comparison of figure 4(d) with the non-electrostatically concentrated actin in figure 4(a). The equatorial peak positions (G and H) deviate slightly from those expected from an exact hexagonal lattice and indicate that the bundled filaments are tightly packed (figure 4(e)). Along the meridional direction, the Bessel function peaks of the native $-13/6$ layer lines of the non-electrostatically concentrated sample (figure 4(c)) have been replaced by a cluster of weaker peaks (J–L) in the multivalent ion condensed sample (figure 4(f)). The peak at $0.136\,\text{Å}^{-1}$ (L) is caused by the mosaic smearing of the strong transverse inter-rod correlation at the same q-value along the equatorial direction, and the intensity agrees well with calculations accounting for the mosaic distribution. The remaining peaks can be completely explained by overtwisting F-actin to a new $-36/17$ symmetry, which corresponds to the $-3.8°$ twist. Experimentally, F-actin is known to exhibit a range of twist states [33, 39, 40], an observation that is consistent

with its low torsional rigidity, as measured with single-molecule techniques [41]. We consider changes in the F-actin helical twist away from its native symmetry by starting with the standard four-sphere model in the $-13/6$ helix and monomer spacing of 28.7 Å (the value extracted from the measurement of actin in figure 4(a)) and twisting the filament over a range of $\pm 10°$ per monomer in increments of $0.05°$. Long repeat helical symmetries up to the 108/51 range have been checked for the appearance of new intense layer lines, and none were found. The measured peaks at $q = 0.115$ and 0.120 Å^{-1} agree well with the $l = 17$ and 19 layer lines of the overtwisted $-36/17$ symmetry (calculated peaks at $q = 0.113$ and 0.120 Å^{-1} after adding mosaic smearing). Even the higher-order feature at $q = 0.227$ Å^{-1} is reproduced.

3. Discussion

It is interesting to examine why the composite polyelectrolyte–counterion system chooses the overtwisted $-36/17$ symmetry. The angle between adjacent monomers on a $-13/6$ helix is given by $-6 \times 2\pi/13$, or $-166.2°$. By contrast, the angle per monomer on a $-36/17$ helix is $-170°$, which indicates the overtwist of $-3.8°$ per monomer. An examination of the local environment around a 1D CDW reveals why the $-36/17$ symmetry is favoured. The packing of helical f-actin rods into a simple columnar hexagonal array will result in interstitial 'channels' through which the CDW can thread. The arrangement of charge within these channels, however, does not match perfectly with a spatially periodic linear CDW and a series of defects is necessarily generated by subdomain 1 of the actin monomer precessing in and out of a given interstitial channel. In twisting from the $-13/6$ to $-36/17$, it can be shown that the density of these defects is greatly reduced [31]. The $-36/17$ symmetry produces evenly spaced negative-charge patches (when projected along z) with a period equal to twice the monomer spacing on a single filament, $d = 57.4$ Å, which is quite close to 59.8 Å, our measured period for the 1D CDW of multivalent ions. In fact, this observed organization of multivalent ions into a classical CDW may be related to the occurrence of these defects. Furthermore, although sd-1 seems to be the most relevant choice as a reference point for making these observations, the same arguments hold true for the entire actin monomer and the entire actin charge distribution.

Optimizing the electrostatic interactions in a single interstitial channel will not necessarily optimize all of the interstitial channels within a hexagonal array of filaments. F-actin is a helix, and the charged patches will precess with a spatial frequency determined by its helical symmetry. As a result, optimizing the charge matching for a CDW threading one channel will not in general optimize charge matching in adjacent channels, since different aspects of the helices will be presented in adjacent tunnels. An examination of this question reveals one other important advantage in changing the actin twist state from $-13/6$ to $-36/17$. There are 36 monomers in the crystallographic repeat of twisted F-actin in the $-36/17$ configuration. The 36 monomers are evenly divisible by six, the number of nearest neighbours in hexagonal coordination, whereas 13, the number of monomers in the native crystallographic repeat of F-actin, is not (figure 5). For F-actin rods with $-36/17$ symmetry organized into a sixfold columnar arrangement, all of the interstitial channels can be optimized simultaneously. A unit cell can be generated with two principal channel arrangements that can be simultaneously optimized, and the entire 2D plane can be tiled with a unit cell without frustration effects. This is clearly not true for $-13/6$ F-actin. Since 13 is not divisible by six nearest neighbours, the pattern of charges presented by helices to adjacent channels depends sensitively on the phase of the actin helices, and it is not possible to tile the 2D surface without frustration.

It is important to assess whether the $-3.8°$ twist which is necessary for the formation of the $-36/17$ helix is forbiddingly large. The torsional rigidity of F-actin has been measured [41]. By using the measured value for the torsional rigidity ($\kappa \approx 8 \times 10^{-26}$ N m^2)
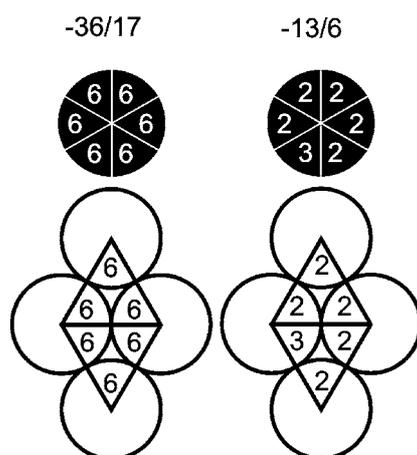
Figure 5. The projection of the F-actin filament monomer structure into a plane perpendicular to the filament axis reveals the relationship between filament symmetry and inter-filament coordination. The number of monomers per repeat length oriented within each of the six 60° sectors is shown on each sector (top diagrams). For example, with the $-36/17$ symmetry, there are 36 monomers per repeat, and they evenly divide into six monomers per 60° sector. In the $-36/17$ case (left), each of the six nearest neighbours facing the filament will interact with the same number of monomers per repeat length. On the other hand, a filament with $-13/6$ symmetry (right) will always have one neighbour inequivalent to the rest. This will have fundamental consequences for hexagonal packing (bottom diagrams). For filaments with $-36/17$ symmetry organized into a hexagonal columnar arrangement, all the channels can be optimized against the CDW simultaneously by aligning the charges on the monomer with the oppositely charged CDW. In contrast, filaments with $-13/6$ symmetry in the same columnar arrangement will have channels that cannot be simultaneously optimized.

and the equipartition theorem, the rms twist of F-actin at room temperature just from thermal fluctuations is of the order of 1° per monomer.

Recent molecular dynamics simulations on realistic representations of F-actin at a spatial resolution comparable to the actin monomer subdomain structure confirm the essential features of our model [42]. For a columnar hexagonal lattice comprised of F-actin helices in the native $-13/6$ twist state, counterions are distributed around F-actin with the symmetry of individual actin helices, while for a lattice of F-actin in the $-36/17$ twist state, counterion distributions rearrange themselves to follow the symmetry of the hexagonal lattice. This supports the experimental observation of a strong CDW state for twisted $-36/17$ F-actin rods.

In the past, a variety of ion species such as Mg^{2+} and Ca^{2+} have been used for the self-assembly of all of the multivalent ion/F-actin phases [15]. In agreement with these findings, we observe the CDW peak in SAXS measurements on partially aligned samples of actin condensed by Mg^{2+} and by Ca^{2+}. These measurements were performed under conditions identical to those of the Ba^{2+} measurements, and the CDW peak is weaker than that for Ba^{2+} in both cases. This indicates that the CDW state is not limited to Ba^{2+} condensed actin bundles, and suggests that it is due to a collective ion organization rather than to an ion-specific binding phenomenon. Although there are approximate trends in the CDW peak intensities for different ion species (e.g. the Ca^{2+} CDW peak appears more intense than the Mg^{2+} CDW peak), they are difficult to quantitatively compare due to the unpredictable amounts of mosaic smearing from different partially aligned samples. Quantitative comparison is also complicated by the shifts in phase boundaries between different condensed phases for different ions [15] (which can potentially vary the number of condensed ions on the polyelectrolyte for a given global ion concentration).

We have performed solid-state NMR experiments on divalent ^{25}Mg ions that comprise the counterion density wave organized within condensed F-actin bundles. Nuclear magnetic resonance (NMR) spectroscopy is a valuable technique for studying ion binding in biological systems. For example ^{43}Ca, ^{25}Mg, ^{113}Cd, ^{23}Na, and ^{39}K NMR have been used to investigate ion binding in proteins such as calmodulin, troponin, and parvalbumin [43, 44]. NMR has also been used to study the interactions of counterions with polyelectrolytes by monitoring quadrupole relaxation of ions with spin $I > 1/2$. ^{25}Mg has a spin-5/2 nucleus with a nuclear quadrupole moment that can relax via interactions with electric field gradients. Measurements of the lineshapes can give insight into the dynamics of Mg^{2+} ions, as well as interactions between Mg^{2+} and F-actin filaments.

Xian *et al* used solution NMR to monitor ^{25}Mg^{2+} counterion dynamics on uncondensed actin filaments [45]. Their results suggest that ^{25}Mg^{2+} rotational correlation times are independent of the rotational dynamics of the actin filaments. Moreover, the competitive binding between ^{25}Mg^{2+} and trivalent cobalt hexamine was directly monitored. However, due to the rapid quadrupole relaxation of the ^{25}Mg^{2+} ($I = 5/2$) and the solid nature of condensed F-actin, solution NMR is not feasible to study the dynamics of ^{25}Mg^{2+} condensed into the CDW state within F-actin bundles, which form at high Mg^{2+} concentrations. In order to gain insight into the dynamics of the counterions within condensed F-actin bundles, we have used solid-state ^{25}Mg NMR techniques, where an accurate determination of longitudinal relaxation times of ^{25}Mg^{2+} in condensed F-actin can be related to correlation times of the counterions through the spectral density.

^{25}Mg isotope enriched MgO was purchased from Oak Ridge National Laboratory (Oak Ridge, TN) and dissolved in HCl to obtain a ^{25}MgCl$_2$ stock solution. Monomeric actin was purified following the method of Spudich and Watt [46] and polymerized using ^{25}MgCl$_2$ to a final concentration of 2 mM. Gelsolin was added at a molar ratio of 1:370 (gelsolin:actin molar ratio) to restrict the length of the F-actin polymers to ~ 1 μm, for comparison with the x-ray results. Phalloidin (Sigma Aldrich, St Louis, MO) was added to prevent depolymerization of actin.

All ^{25}Mg NMR experiments were carried out at 45.898 MHz on a 17.5 T Oxford Instruments (Witney, UK) 750 MHz magnet controlled by a Varian (Palo Alto, CA) Unity Inova operating system. Solution NMR experiments employed a Varian 10 mm 15N-31P BB solution probe while the solid-state NMR experiments used a Doty Scientific (Columbia, SC) XC5 15N-31P CPMAS solid probe. A 90° pulse width of 22 μs was used along with a 100 μs post-acquisition delay time. Longitudinal relaxation times were measured by both inversion recovery and saturation recovery methods. Magic angle spinning (MAS) experiments were performed at a rotation rate of 2 kHz. Solid-state NMR samples were prepared by centrifuging F-actin bundles into Doty Scientific 5 mm XC5 sealing cells and removing excess supernatant, in order to maximize the signal from the ^{25}Mg in the bundles.

Figure 6 shows the solution NMR spectra of F-actin filaments (10 mg ml^{-1}) in the uncondensed phase with 2 mM ^{25}MgCl$_2$ (figure 6(a)) and the condensed bundle phase with 30 mM ^{25}Mg (figure 6(b)). In both cases, a sharp component of the NMR signal corresponding to relaxation of ^{25}Mg in the supernatant is visible. The uncondensed sample exhibits a lineshape and linewidth comparable to that from the measurements of Xian *et al* [45]. Moreover, in figure 6(a), the broad components due to the ^{25}Mg condensed on F-actin filaments are clearly visible in the sample at 2 mM MgCl$_2$. These broad components disappear at 30 mM MgCl$_2$ as expected (figure 6(b)). The relaxation in the condensed Mg^{2+} within actin filament bundles is estimated to be more 'solid like' and therefore faster than that of the excess Mg^{2+} dissolved in the supernatant, hence the NMR signal of the Mg^{2+} is significantly broader. Moreover, in the sample with 30 mM Mg^{2+}, the solution signal overwhelms the solid-state signal due to the
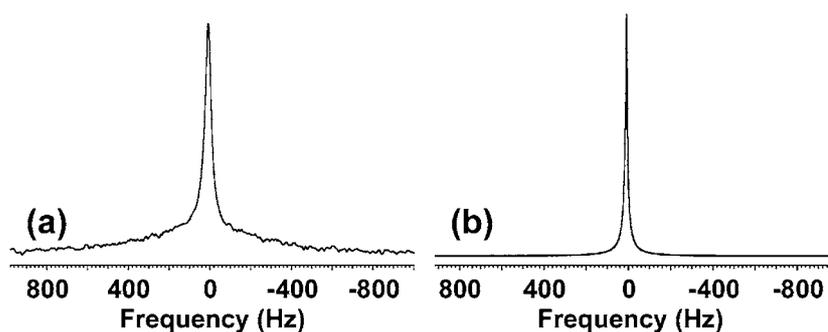
Figure 6. (a) ^{25}Mg NMR spectrum of 2 mM Mg^{2+} in 10 mg ml^{-1} F-actin solution. The F-actin is uncondensed. (b) ^{25}Mg NMR spectrum of 30 mM Mg^{2+} in condensed 10 mg ml^{-1} F-actin solution. F-actin is condensed into a bundled phase by the Mg^{2+} ions. The solution Mg signal is large compared to the solid-state Mg signal.
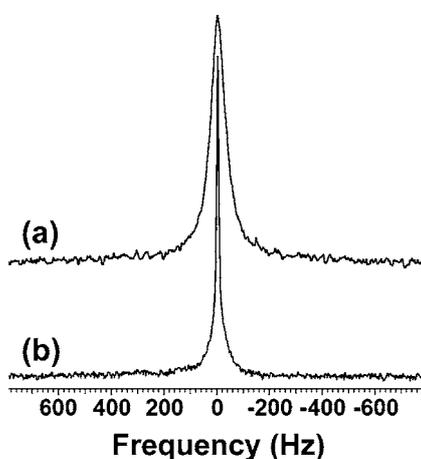
Figure 7. ^{25}Mg NMR spectrum of 30 mM Mg^{2+} in condensed 10 mg ml^{-1} F-actin in the solid state: (a) static solid-state spectrum (b) 2 kHz magic angle spinning spectrum.

large number of ions remaining in solution, so it is not possible to use solution NMR to probe the dynamics of the condensed Mg^{2+} ions. In order to access the dynamics of the condensed Mg^{2+} ions within the F-actin bundles, we isolated the pellet of Mg^{2+} condensed actin bundles, and employed magic angle spinning (MAS) NMR, which is often used to improve sensitivity and resolution in solid-state samples. In MAS, the samples are rapidly rotated around an axis at the 'magic angle' θ_m to the external magnetic field in order to average anisotropic terms to zero [47, 48]. Thus, the magic angle is defined by $3\cos^2\theta_m - 1 = 0$ which is approximately $54.736°$. Representative solid-state NMR spectra are shown in figure 7. The static ^{25}Mg spectrum of F-actin condensed by 30 mM MgCl$_2$ (figure 7(a)) has a static line width of approximately 75 Hz. The MAS spectrum of the same sample is shown in figure 7(b), with a linewidth of $\sim$9 Hz. Inversion and saturation recovery experiments were performed on condensed F-actin in the solid state, as well as on MgCl$_2$ standard and on G-buffer containing 30 mM MgCl$_2$ to obtain preliminary longitudinal relaxation rates. For the ^{25}MgCl$_2$ standard, we found the longitudinal lifetime T_1 varies from 100 to 150 ms as the temperature is increased from 4 to 38 °C. For ^{25}Mg in a non-polymerizing G-actin buffer, we found T_1 to vary in a

similar manner, from 62 to 96 ms as a function of temperature ranging from 4 to 38 °C. This is expected since Mg can be chelated by ATP in the solution. For condensed F-actin, however, we find that T_1 decreases to a range from 11 to 15 ms over the same temperature range. From our x-ray measurements presented above, we see that divalent ions are organized into CDWs within F-actin bundles. The preliminary NMR results presented here give a quantitative measure for the decreased mobility of Mg^{2+} ions condensed within F-actin bundles, compared to Mg^{2+} ions dissolved in the supernatant. In this context, it is interesting to note that the value of T_1 for Mg^{2+} ions in the CDW is intermediate between typical liquid-like and solid-like values.

4. Conclusion

We have experimentally examined the mechanism for like-charge attraction in cytoskeletal F-actin and found evidence for counterion organization. The microscopic mechanism involves a coupled mode between a counterion CDW and the polyelectrolyte twist. (The counterion CDW cannot exist without the polyelectrolyte twist and vice versa.) This implies that within a bundle, it is possible for many actin filaments to collectively twist by *the same amount* in concert, in response to binding by crosslinking agents (divalent ions in the present case). This coupling between filament twist and linker binding may have biological implications. For example, it has been observed that the actin binding protein cofilin can change the twist state of individual actin filaments [49]. Similar compromises between F-actin twist and F-actin crosslinking by actin binding proteins within bundles can influence the hierarchy of existing interactions by local modifications of binding sites and impinge on cytoskeletal regulation. We have also directly measured the dynamics of the ions condensed within actin bundles by using magic angle spinning solid-state NMR. We find that their longitudinal relaxation time decreases by approximately an order of magnitude relative to ions in free solution. It is known that different polyelectrolytes require ions of different valences to condense, and an experimentally motivated criterion for the degree of ion multivalence required for generating attractions has been recently proposed [18]. We plan to extend this preliminary NMR investigation by obtaining relaxation data at several field strengths and for ions of different valences.

References

[1] Gelbart W M, Bruinsma R F, Pincus P A and Parsegian V A 2000 *Phys. Today* **53** 38–44
[2] Israelachvili J 1992 *Intermolecular and Surface Forces* 2 edn (London: Academic)
[3] Evans D R and Wennerstrom H 1999 *The Colloidal Domain* 2 edn (New York: Wiley)
[4] Nelson P 2004 *Biological Physics* (New York: Freeman)
[5] Derjaguin B V and Landau L 1941 *Acta Physicochimica (URSS)* **14** 633
[6] Verwey E J and Overbeek J T G 1948 *Theory of the Stability of Lyophobic Colloids* (Amsterdam: Elsevier)

[7] LeBret M and Zimm B H 1984 *Biopolymers* **23** 287–312
[8] Kirkwood J G and Shumaker J B 1952 *Proc. Natl Acad. Sci. USA* **38** 863–71
[9] Oosawa F 1968 *Biopolymers* **6** 1688
[10] Ray J and Manning G S 1994 *Langmuir* **10** 2450–61
[11] Deserno M, Arnold A and Holm C 2003 *Macromolecules* **36** 249–59
[12] Tang J X and Janmey P A 1996 *J. Biol. Chem.* **271** 8556–63
[13] Tang J X, Wong S, Tran P T and Janmey P A 1996 *Ber. Bunsenges. Phys. Chem.* **100** 796–806
[14] Borukhov I, Bruinsma R F, Gelbart W M and Liu A J 2001 *Phys. Rev. Lett.* **86** 2182–5
[15] Wong G C L, Lin A, Tang J X, Li Y, Janmey P A and Safinya C R 2003 *Phys. Rev. Lett.* **91** 018103
[16] Borukhov I and Bruinsma R 2001 *Phys. Rev. Lett.* **87** 158101
[17] Deng H and Bloomfield V A 1999 *Biophys. J.* **77** 1556–61
[18] Butler J C, Angelini T E, Tang J X and Wong G C L 2003 *Phys. Rev. Lett.* **91** 028301
[19] Borukhov I, Lee K C, Bruinsma R F, Gelbart W M, Liu A J and Stevens M J 2002 *J. Chem. Phys.* **117** 462–80
[20] Ha B-Y and Liu A J 1997 *Phys. Rev. Lett.* **79** 1289–92
[21] Ha B-Y and Liu A J 1998 *Phys. Rev. Lett.* **81** 1011–4
[22] Podgornik R and Parsegian V A 1998 *Phys. Rev. Lett.* **80** 1560–3
[23] Golestanian R and Liverpool T B 2002 *Phys. Rev.* E **66** 051802
[24] Rouzina I and Bloomfield V A 1996 *J. Phys. Chem.* **100** 9977–89
[25] Grønbech-Jensen N, Mashl R J, Bruinsma R F and Gelbart W M 1997 *Phys. Rev. Lett.* **78** 2477–80
[26] Shklovskii B I 1999 *Phys. Rev. Lett.* **82** 3268–871
[27] Kornyshev A A and Leikin S 1999 *Phys. Rev. Lett.* **82** 4138–41
[28] Solis F J and Olvera de la Cruz M 1999 *Phys. Rev.* E **60** 4496
[29] Arenzon J J, Stilck J F and Levin Y 1999 *Eur. Phys. J.* B **12** 79
[30] Diehl A, Carmona H A and Levin Y 2001 *Phys. Rev.* E **6401** 1804 (1 part 1)
[31] Angelini T E, Liang H, Wriggers W and Wong G C L 2003 *Proc. Natl Acad. Sci. USA* **100** 8634–7
[32] Lodish H, Berk A, Zipursky S L, Matsudaira P, Baltimore D and Darnell J 2000 *Molecular Cell Biology* 4th edn
      (New York: Freeman)
[33] Sheterline P, Clayton J and Sparrow J C 1998 *Actin* (New York: Oxford University Press)
[34] Al-Khayat H A, Yagi N and Squire J M 1995 *J. Mol. Biol.* **252** 611–32
[35] Janmey P A, Peetermans J, Zaner K S, Stossel T P and Tanaka T 1986 *J. Biol. Chem.* **261** 8357–62
[36] Holmes K C, Popp D, Gebhard W and Kabsch W 1990 *Nature* **347** 44–9
[37] Tibbits T T and Caspar D L D 1993 *Acta Crystallogr.* A **49** 532–45
[38] Coridan R H, Angelini T E, Sanders L K, Xian W and Wong G C L 2004 unpublished results
[39] Egelman E H, Francis N and DeRosier D J 1982 *Nature* **298** 131–5
[40] Aebi U, Millonig R, Salvo H and Engel A 1986 *Ann. New York Acad. Sci.* **483** 100–19
[41] Tsuda Y, Yasutake H, Ishijima A and Yanagida T 1996 *Proc. Natl Acad. Sci. USA* **93** 12937–42
[42] Lee J and Luijten E 2004 unpublished results
[43] Forsen S and Lindman B 1981 *Annual Reports on NMR Spectroscopy* ed G Webb (New York: Academic)
      pp 183–226
[44] Forsen S and Vogel H J 1987 *Biological Magnetic Resonance* ed L Berliner and J Reubin (New York: Plenum)
      pp 249–309
[45] Xian W, Tang J X, Janmey P A and Braunlin W H 1999 *Biochemistry* **38** 7219–26
[46] Spudich J and Watt S 1971 *J. Biol. Chem.* **246** 4866–71
[47] Andrew E R 1959 *Arch. Sci.* **12** 103–8
[48] Lowe I J 1959 *Phys. Rev. Lett.* **2** 285–7
[49] McGough A, Pope B, Chiu W and Weeds A 1997 *J. Cell. Biol.* **138** 771–81